

# NON-GAUSSIAN ERROR CONTRIBUTION TO LIKELIHOOD ANALYSIS OF THE MATTER POWER SPECTRUM

RYUICHI TAKAHASHI<sup>1</sup>, NAOKI YOSHIDA<sup>3</sup>, MASAHIRO TAKADA<sup>3</sup>, TAKAHIKO MATSUBARA<sup>2</sup>, NAOSHI SUGIYAMA<sup>2,3</sup>, ISSHA KAYO<sup>3</sup>, TAKAHIRO NISHIMICHI<sup>4</sup>, SHUN SAITO<sup>4</sup>, ATSUSHI TARUYA<sup>3,5</sup>

<sup>1</sup> Faculty of Science and Technology, Hirosaki University, 3 bunkyo-cho, Hirosaki, Aomori, 036-8561, Japan

<sup>2</sup> Department of Physics, Nagoya University, Chikusa, Nagoya 464-8602, Japan

<sup>3</sup> Institute for the Physics and Mathematics of the Universe, The University of Tokyo, 5-1-5 Kashiwa-no-ha, Kashiwa, Chiba 277-8568, Japan

<sup>4</sup> Department of Physics, School of Science, The University of Tokyo, Tokyo 113-0033, Japan and

<sup>5</sup> Research Center for the Early Universe, The University of Tokyo, Tokyo 133-0033, Japan

*Draft version October 27, 2019*

## ABSTRACT

We study the sample variance of the matter power spectrum for the standard  $\Lambda$  Cold Dark Matter universe. We use a total of 5000 cosmological  $N$ -body simulations to study in detail the distribution of best-fit cosmological parameters and the baryon acoustic peak positions. The obtained distribution is compared with the results from the Fisher matrix analysis with and without including non-Gaussian errors. For the Fisher matrix analysis, we compute the derivatives of the matter power spectrum with respect to cosmological parameters using directly full nonlinear simulations. We show that the non-Gaussian errors increase the unmarginalized errors by up to a factor 5 for  $k_{\text{max}} = 0.4h/\text{Mpc}$  if there is only one free parameter provided other parameters are well determined by external information. On the other hand, for multi-parameter fitting, the impact of the non-Gaussian errors is significantly mitigated due to severe parameter degeneracies in the power spectrum. The distribution of the acoustic peak positions is well described by a Gaussian distribution, with its width being consistent with the statistical interval predicted from the Fisher matrix. We also examine systematic bias in the best-fit parameter due to the non-Gaussian errors. The bias is found to be smaller than the  $1\sigma$  statistical error for both the cosmological parameters and the acoustic scale positions.

*Subject headings:* cosmology: theory – large-scale structure of universe

## 1. INTRODUCTION

The baryon acoustic oscillation (BAO) is imprinted in the distribution of galaxies as is found in the temperature fluctuations in the cosmic microwave background. The acoustic length scale is determined by the sound horizon of the photon-baryon fluid at recombination epoch; it can thus be used as a standard ruler which provides us with a robust method to measure distance scales out to essentially any epoch (e.g., Eisenstein et al. 1998; Blake & Glazebrook 2003; Seo & Eisenstein 2003; Matsubara 2004; Guzik et al. 2007). Using the observed distance-redshift relation, we can obtain an accurate cosmic expansion history, which in turn gives strong constraints on the nature of dark energy. The large-area galaxy surveys such as two-degree Field Survey (2dF) and Sloan Digital Sky Survey (SDSS) detected the BAO signature in the galaxy distribution (Cole et al. 2005; Eisenstein et al. 2005; Percival et al. 2007; Okumura et al. 2008; Gaztanaga et al. 2008; Sanchez et al. 2009). The latest result of the SDSS DR7 showed a constraint on the distance to a redshift  $z = 0.28$  within 2.7% accuracy (Percival et al. 2009; Reid et al. 2009; Kazin et al. 2009). Future and ongoing surveys such as the Baryon Oscillation Spectroscopic Survey (BOSS)<sup>1</sup>, the Hobby-Eberly Dark Energy Experiment (HETDEX)<sup>2</sup>, and the WiggleZ surveys<sup>3</sup> will measure the distance to higher redshifts within a few percent accuracy.

The BAO signature appears as a small wiggle pattern in the galaxy power spectrum. Since the amplitude of BAO wiggle is very small ( $\sim$  a few percent), rather accurate theoretical models are needed. Especially, in order to determine the distance within a percent accuracy for the planned or ongoing surveys, we need to be able to predict the acoustic scale with much higher accuracies ( $\sim 0.1\%$ ). However, there are complicated astrophysical processes such as the non-linear gravitational evolution, scale-dependent bias of galaxies, redshift space distortion, and the effect of massive neutrino. Many authors tackled these problems using numerical simulations (Meiksin et al. 1999; Seo & Eisenstein 2005; Huff et al. 2007; Smith, Scoccimarro & Sheth 2007, 2008; Angulo et al. 2008; Takahashi et al. 2008; Seo et al. 2008; Nishimichi et al. 2009; Kim et al. 2009; Heitmann et al. 2009) and analytical perturbation theories (Crocce & Scoccimarro 2006, 2008; Jeong & Komatsu 2006, 2009; Nishimichi et al. 2007; McDonald 2007; Matarrese & Pietroni 2007, 2008; Eisenstein et al. 2007; Pietroni 2008; Matsubara 2008a,b; Taruya & Hiramatsu 2008; Takahashi 2008; Nomura et al. 2008; Rassat et al. 2008; Sanchez et al. 2008; Padmanabhan & White 2008; Saito, Takada & Taruya 2009; Shoji, Jeong & Komatsu 2009; Taruya et al. 2009).

It is crucial to use not only accurate power spectra but also accurate covariance matrices in order to determine cosmological parameters from the galaxy power spectrum. If the matter density fluctuations obey a Gaussian distribution, the covariance matrix has only diagonal element and the relative error is simply given by the

<sup>1</sup> <http://www.sdss3.org/cosmology.php>

<sup>2</sup> <http://hetdex.org/>

<sup>3</sup> <http://wigglez.swin.edu.au/Welcome.html>

square root of the number of modes in the survey area (e.g. Feldman, Kaiser & Peacock 1994). However, when the density fluctuations grow to the non-linear regime, the mode coupling between different wavenumbers generates non-zero off-diagonal elements, and the so-called non-Gaussian error is induced (e.g. Scoccimarro, Zaldarriaga & Hui 1999; Meiksin & White 1999). Rimes & Hamilton (2005, 2006) first pointed out that there is little information contained in the power spectrum at quasi-nonlinear regime ( $k = 0.2 - 0.8h/\text{Mpc}$ ) due to the non-Gaussian error (see also Hamilton, Rimes & Scoccimarro 2006; Neyrinck, Szapudi & Rimes 2006; Neyrinck & Szapudi 2007, 2008; Lee & Pen 2008; Neyrinck, Szapudi & Szalay 2009; Lu, Pen & Dore 2009; Sato et al. 2009). For weak lensing (cosmic shear) analysis, the non-Gaussian error contribute the total error substantially (Cooray & Hu 2001; Sefusatti et al. 2006; Dore, Lu & Pen 2009; Takada & Jain 2009; Pielorz et al. 2009), but also may systematically shift the best fitting parameter (Hartlap et al. 2009; Ichiki et al. 2009). Especially, if there are a small number of parameters to be determined, the non-Gaussianity affects the errors significantly (see the discussion in Takada & Jain 2009).

In our previous paper (Takahashi et al. 2009, hereafter T09), we used 5000 cosmological simulations to obtain the accurate covariance matrix of the matter power spectrum. This is a largest number of realizations ever done for the cosmological N-body simulation. We studied the non-Gaussian error contribution to the signal-to-noise ratio for the measurement of the power spectrum, and found that the non-Gaussian error is important at small length-scale  $k > 0.2h/\text{Mpc}$ . In this paper, we further investigate the non-Gaussian error contribution to the cosmological parameter estimation and the best-fit values using the  $\chi^2$  likelihood analysis. We calculate the distribution of the best-fit parameters among the 5000 realizations, and compare it with the results using the Fisher matrix analysis. We also study the distribution of the acoustic scale positions among the realizations. Our results in this paper can be used not only for the BAO analysis but also for the more general issue in the likelihood analysis of the non-linear matter power spectrum.

Throughout the present paper, we adopt the standard  $\Lambda\text{CDM}$  model with matter density  $\Omega_m = 0.238$ , baryon density  $\Omega_b = 0.041$ , dark energy density  $\Omega_w = 0.762$  with equation of state  $w = -1$ , spectral index  $n_s = 0.958$ , amplitude of fluctuations  $\sigma_8 = 0.76$ , and expansion rate at the present time  $H_0 = 73.2 \text{ km s}^{-1} \text{ Mpc}^{-1}$ , consistent with the 3-year WMAP results (Spergel et al. 2007).

## 2. MATTER POWER SPECTRUM AND ITS COVARIANCE MATRIX FROM NUMERICAL SIMULATIONS

We follow the gravitational evolution of  $256^3$  collisionless dark matter particles in a volume of  $1000h^{-1}\text{Mpc}$  on a side using the cosmological simulation code Gadget-2 (Springel, Yoshida & White 2001; Springel 2005). We generate initial conditions following the standard Zel'dovich approximation using the matter transfer function calculated by CAMB (Code for Anisotropies in the Microwave Background: Lewis, Challinor & Lasenby 2000; also see Seljak & Zaldarriaga 1996). The initial redshift is set to be  $z = 20$ . We use outputs at  $z = 3, 1$  and 0. To calculate the density fluctuations, we assign the N-body particles onto a  $512^3$  rectangular grid using the

cloud-in-cell scheme. Then we perform the Fourier transform and calculate the power spectrum in both real space and redshift space. We run 5000 Particle-Mesh(PM) simulations to follow the non-linear evolution of the power spectrum and its covariance matrix in detail. We have checked that the power spectra of our simulations agree well with the result of the higher resolution TreePM simulation, within 1(3)% for  $k < 0.2(0.4)h/\text{Mpc}$  (here the Nyquist wavenumber is  $k = 0.8h/\text{Mpc}$ ). If the initial redshift is set to be higher,  $z = 50$ , the results agree within 2(10)% for  $k < 0.2(0.4)h/\text{Mpc}^4$ . This is a sufficient accuracy for our purpose, which is to investigate the non-linear evolution of the power spectrum at BAO scales.

Denoting  $\hat{P}_i(k)$  as the power spectrum computed from the  $i$ -th realization, the ensemble averaged power spectrum is estimated from the mean of the power spectra between 5000 realizations:

$$\bar{P}(k) = \frac{1}{N_r} \sum_{i=1}^{N_r} \hat{P}_i(k), \quad (1)$$

where  $N_r = 5000$ , the number of our realizations. Similarly, the covariance matrix between the spectra of  $k_1$  and  $k_2$  is estimated as

$$\text{cov}(k_1, k_2) = \frac{1}{N_r - 1} \sum_{i=1}^{N_r} \left[ \hat{P}_i(k_1) - \bar{P}(k_1) \right] \left[ \hat{P}_i(k_2) - \bar{P}(k_2) \right]. \quad (2)$$

The accuracy of the covariance is analytically estimated for the Gaussian density fluctuations (see Appendix). For example, the relative errors in the diagonal covariance terms are found to scale with the number of realizations as  $(2/N_r)^{1/2}$ ; our 5000 simulations provide a few percent accuracy. Clearly, our study achieves an unprecedented accuracy of the covariance matrix estimation on BAO scales.

The power spectrum covariance is formally expressed as a sum of the two contributions, the Gaussian and non-Gaussian terms (e.g. Scoccimarro, Zaldarriaga & Hui 1999; Meiksin & White 1999):

$$\begin{aligned} \text{cov}(k_1, k_2) &\equiv \left\langle \left( \hat{P}(k_1) - P(k_1) \right) \left( \hat{P}(k_2) - P(k_2) \right) \right\rangle \\ &= \frac{2}{N_{k_1}} P^2(k_1) \delta_{k_1, k_2}^K + \frac{1}{V} \int_{|\mathbf{k}'_1| \in k_1} \int_{|\mathbf{k}'_2| \in k_2} \frac{d^3 \mathbf{k}'_1}{V_{k_1}} \frac{d^3 \mathbf{k}'_2}{V_{k_2}} \\ &\quad \times T(\mathbf{k}'_1, -\mathbf{k}'_1, \mathbf{k}'_2, -\mathbf{k}'_2). \end{aligned} \quad (3)$$

The first term arises from the Gaussian fluctuations, while the second term is the non-Gaussian error arising from the mode coupling during the non-linear evolution. Here,  $P(k) = \langle \hat{P}(k) \rangle$  is the mean power spectrum,  $T$  is the trispectrum, the integral is done over the shell of the radius  $k_{1,2}$  with the width  $\Delta k$  in Fourier space, and  $V_{k_{1,2}}$  is the volume of the shell given by  $V_k = 4\pi k^2 \Delta k$ . The expression in Eq.(3) depends on the bin width, the first term is proportional to  $1/(V\Delta k)$ , while the second term is  $\propto 1/V$ . Hence, for the finer bin width, the impact of the Gaussian term becomes relatively enhanced. Note

<sup>4</sup> The agreement is achieved in real space. In redshift space, PM simulations somewhat underestimate the power spectrum at small scales ( $k = 0.4h/\text{Mpc}$ ) by 20%.

however that the parameter estimation shown in the following is independent of the bin width. Throughout this paper, the bin width is set to  $\Delta k = 0.01h/\text{Mpc}$ .<sup>5</sup>

In this paper, we do not consider another non-Gaussian term in Eq.(3) arising from the finite survey volume (the so-called beat-coupling effect; Rimes & Hamilton 2006). Fluctuations with wavelength larger than the survey region may contribute to the covariance on smaller scale. Although this effect can increase the covariance by over ten percent (T09), the main conclusions we draw in the present paper remain robust to the uncertainty.

### 3. EFFECTS OF NON-GAUSSIAN ERROR ON LIKELIHOOD ANALYSIS OF COSMOLOGICAL PARAMETERS

#### 3.1. Parameter Estimation for Cosmological Parameters

In this section, we study the effects of the non-Gaussian errors on the cosmological parameter estimation given the power spectrum measured from a hypothetical survey of  $(1h^{-1}\text{Gpc})^3$  volume. We use the Fisher matrix formalism to estimate the accuracy of parameter estimation<sup>6</sup> (Tegmark, Taylor & Heavens 1997):

$$F_{ij} = \sum_{k_{1,2} < k_{\text{max}}} \text{cov}^{-1}(k_1, k_2) \left. \frac{\partial P(k_1; \mathbf{x})}{\partial \ln x_i} \right|_{\text{fid}} \left. \frac{\partial P(k_2; \mathbf{x})}{\partial \ln x_j} \right|_{\text{fid}}. \quad (4)$$

where  $x_i$  denotes cosmological parameters, and the partial derivative such as  $\partial P/\partial x_i$  is evaluated around the fiducial model. We include 5 parameters (therefore  $i = 1, 2, \dots, 5$ ): the primordial power spectrum parameters,<sup>7</sup> the normalization parameter  $A_s$  (not  $\sigma_8$ ) and the spectral index  $n_s$ , the baryon density  $\Omega_b h^2$ , the dark matter density  $\Omega_c h^2$ , and the dark energy equation of state parameter  $w$ . We assume a flat universe throughout the present paper. In Eq. (4) we use  $\ln x_i$  (not  $x_i$ ) as the variables such that the Fisher matrix gives the relative accuracy of a given parameter estimation: the marginalized error is then given as  $\Delta x_i/x_i = (F^{-1})_{ii}^{1/2}$ . Note that for  $w$ , which has a negative value for the fiducial value, we simply compute  $w \partial \ln P / \partial w$  for the derivative. From Eqs.(3) and (4), the estimation error  $\Delta x_i/x_i$  is inversely proportional to the survey volume as  $\Delta x_i/x_i \propto V^{-1/2}$ .

We need to compute the derivatives of the power spectrum to compute the Fisher matrix in Eq. (4). For each cosmological parameter, we ran simulations with one parameter slightly varied, while fixing other parameters to the fiducial values. We then compute the derivatives by the two-side differences of steps  $\Delta x_i/x_i = \pm 0.05$ . We use 40 realizations are used for each parameter variation. Fig.1 shows the derivatives of the power spectrum with respect to each cosmological parameter in real space (left column) and in redshift space (right column), respectively. The symbols are our simulation results: the red circles are for  $z = 0$ , the blue triangles for  $z = 1$ , and the green crosses for  $z = 3$ , respectively. The sensitivity of the power spectrum to cosmological parameters

appears differently between in real- and redshift-space, due to the redshift distortion effects. For example, for a model with higher power spectrum normalization i.e. larger  $A_s$ , the power spectrum amplitudes are increasingly enhanced at larger  $k$  due to the stronger nonlinearities in real space. In redshift space, however, the enhancement is significantly suppressed by the stronger finger-of-God effect, which arises from random velocity dispersion of dark matter particles in nonlinear objects. The relative amplitude of baryon acoustic oscillations is enhanced with increasing the baryon density. Finally, a change in  $w$  affects the power spectrum via the effect on the growth rate. We naively expect that the dependence of  $P(k)$  on  $w$  becomes scale-dependent in the nonlinear regime. However, the induced scale-dependence is weak and the dark energy parameter is very likely degenerated with the galaxy bias in the measured galaxy power spectrum.

The simulation results are compared with the analytical predictions computed from the linear theory (the dashed curve) and the halofit (the short-dashed curve: Smith et al. 2003), respectively.<sup>8</sup> The redshift-space power spectrum derivatives are compared with the linear theory. In the linear power spectrum in redshift space, we use the Kaiser approximation and do not include the Finger-of-God term. All the analytical predictions agree well with the simulation results at small  $k$ . In particular, the halofit agrees with the simulations to within 10% accuracy.

In our previous paper (T09), we studied the impact of the non-Gaussian error on the signal-to-noise ratio of power spectrum measurement:

$$\left( \frac{S}{N} \right)^2 = \sum_{k_{1,2} < k_{\text{max}}} \text{cov}^{-1}(k_1, k_2) P(k_1) P(k_2). \quad (5)$$

It was found that, in the linear regime, the  $S/N$  keeps increasing with increasing the maximum wavenumber  $k_{\text{max}}$  as  $(S/N) \propto k_{\text{max}}^{3/2}$ . However the  $S/N$  saturates at some  $k_{\text{max}}$  in the weakly nonlinear regime, and stays nearly constant at larger  $k_{\text{max}} > 0.2h/\text{Mpc}$  due to the non-Gaussian errors. From these results one may naively guess that the parameter estimation is also significantly affected by the non-Gaussian errors when the power spectrum information to the larger  $k_{\text{max}}$  is included. In the following, we will study the impact of the non-Gaussian errors on the parameter estimation.

Fig.2 shows the marginalized error on each parameter,  $\Delta x_i/x_i = (F^{-1})_{ii}^{1/2}$ , as a function of  $k_{\text{max}}$ , where the power spectrum information up to a given  $k_{\text{max}}$  is included. In each panel the symbols show the simulation results including the full covariance matrix. The simulation results are almost indistinguishable from the solid curves that are computed only by including the Gaussian error covariances, computed from simulations, in Eq. (3). The agreement indicates that the Gaussian error assumption actually provides a good approximation for the pa-

<sup>5</sup> We also try the half bin-width,  $\Delta k = 0.005h/\text{Mpc}$ , but our results in the following sections are almost same.

<sup>6</sup> Here, we do not consider the Alcock-Paczynski effect (Alcock & Paczynski 1979) which would affect the measurement accuracy for the dark energy.

<sup>7</sup> We assume the primordial power spectrum given as  $P_0(k) \propto A_s^2(k/k_0)^{n_s}$ , where the pivot wavenumber  $k_0$  is set to  $k_0 = 0.002/\text{Mpc}$  as employed by Komatsu et al. (2009).

<sup>8</sup> We also compare the Lagrangian perturbation theory (LPT: Matsubara 2008a) with the simulation results in the manuscript in previous version (Takahashi et al. arXiv:0912.1381v1). For the redshift-space spectrum, the LPT agrees well with the simulations at small  $k$ , but deviates significantly in the weakly nonlinear regime due to a too significant exponential damping,  $P_{\text{LPT}}(k) \propto \exp[-\text{const.} \times k^2]$  (Matsubara 2008a).

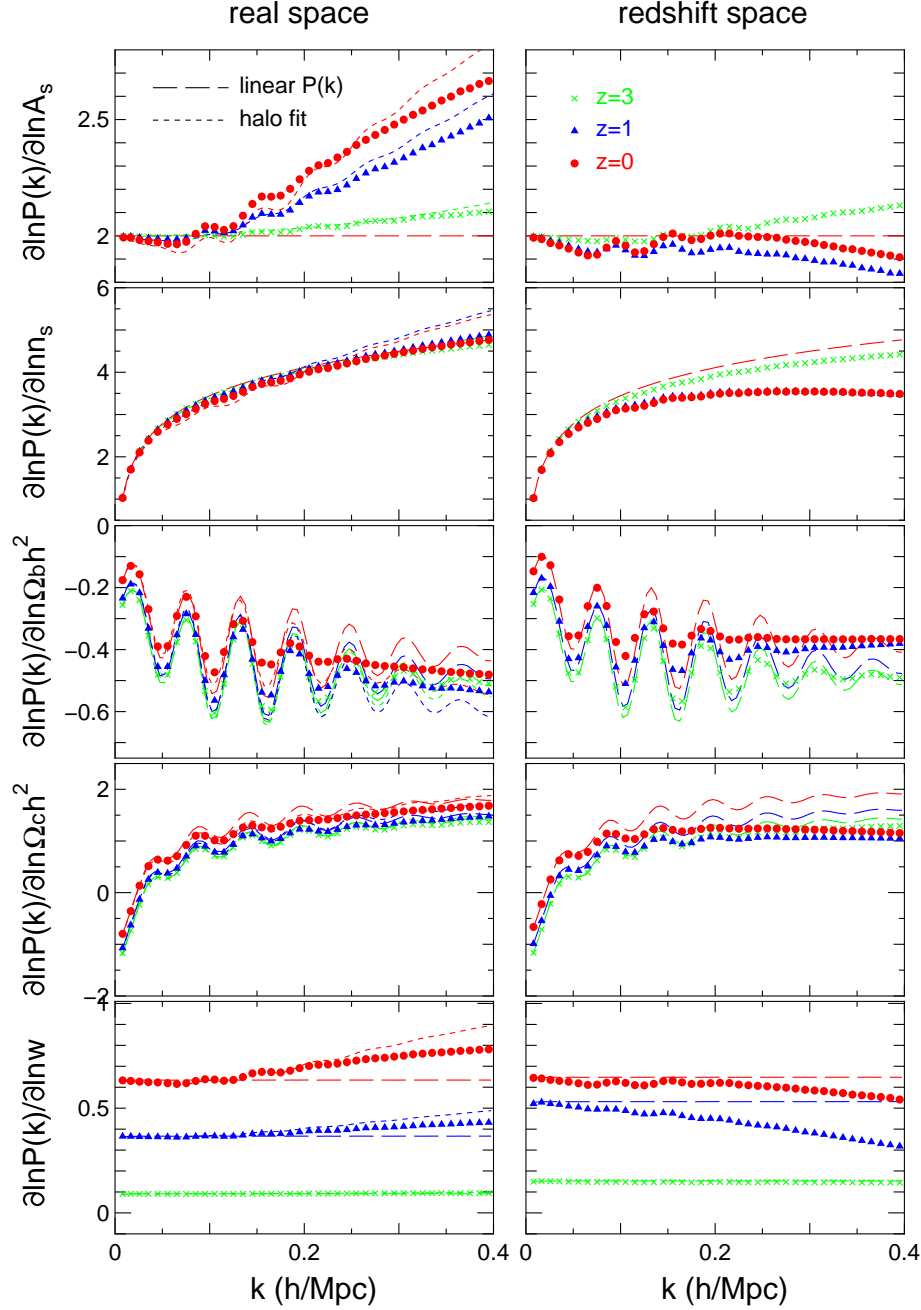


FIG. 1.— The derivatives of non-linear power spectrum with respect to cosmological parameters ( $A_s, n_s, \Omega_b h^2, \Omega_c h^2, w$ ) in real-space (left panel) and redshift-space (right). The cross, triangle and circle symbols show the simulation results at redshifts  $z = 3, 1$  and  $0$ , respectively. The dashed curves are the linear theory predictions, the dotted curves are for the halo fit.

parameter estimation over scales of interest, even though the non-Gaussian errors have a significant impact on the  $S/N$  at  $k_{\max} > 0.2 h/\text{Mpc}$ . A more quantitative interpretation of these results will be given later. For comparison, the dashed and dotted curves show the results obtained by using the linear theory and halo fit to estimate the power spectrum as well as the Gaussian error covariances. These analytical predictions are far from the simulation results due to their inaccuracies in comparison with the simulations. Although the power spectrum and its derivatives in the halo fit agree within  $\sim 10\%$  with the simulations (see Fig.1), the parameter estimations

are largely different as shown in Fig.2. This is because when calculating the inverse matrix of the Fisher matrix, even a small errors in the Fisher matrix generates large errors in the inverse matrix.

Fig.3 shows the relative accuracies of each parameter estimation as a function of  $k_{\max}$ . There, we compare the results derived from the covariances with and without the non-Gaussian error contributions. The solid curves are the results where all the five parameters are included in the Fisher analysis, while the dashed curve shows the unmarginalized error on each parameter, i.e., the error is obtained by considering only one pa-

parameter,  $\Delta x_i/x_i = F_{ii}^{-1/2}$ . In other words, the dashed curves correspond to the case where other parameters are well constrained by external data sets. The difference between the solid and dashed curves is caused by the parameter degeneracies; the marginalized error becomes same as the unmarginalized error when the parameters are independent in the measured power spectrum. It is clear that, for the unmarginalized errors, including the non-Gaussian covariances degrades the parameter errors by a factor 4-5 for the redshift  $z = 0$ , and by a factor 2-3 for  $z = 1$ , respectively. The level of the degradation is similar to that of the  $S/N$  as found in T09. Therefore, the impact of non-Gaussian covariance errors is significantly mitigated by the parameter degeneracies (see also, Neyrinck & Szapudi 2007; Takada & Jain 2009). The degradation of  $S/N$  increases the full Fisher ellipsoid volume, and then individual parameters are not tightly constrained due to the parameter degeneracies in such a high-dimension parameter space.

In the upper two panels for  $A_s$  and  $n_s$  the short dashed curves show the results for the two parameter fitting case ( $A_s, n_s$ ), which are very similar to the solid curves. In reality, parameters that describe galaxy bias need to be further included. We thus conclude that the impact of the non-Gaussian errors is less important than the parameter degeneracies, and that the Gaussian covariances can provide a good approximation to obtain the statistical uncertainty of given parameters.

### 3.2. Distribution of Best-Fit Parameters

Nonlinear structure formation causes non-Gaussian distributions of the power spectrum estimators at small scales, as studied in, e.g., T09, in detail. Here, utilizing our 5000 realizations, we quantify the distribution of parameter estimation taking into account the non-Gaussian covariances and the marginalization over other parameters. To this end, we simply use the  $\chi^2$ -fitting analysis given as

$$\chi_i^2(\mathbf{x}) = \sum_{k_1, k_2 < k_{\max}} \text{cov}^{-1}(k_1, k_2) \left[ P(k_1; \mathbf{x}) - \hat{P}_i(k_1) \right] \times \left[ P(k_2; \mathbf{x}) - \hat{P}_i(k_2) \right], \quad (6)$$

where  $\mathbf{x} = (A_s, n_s, \Omega_b h^2, \Omega_c h^2, w)$ ,  $\hat{P}_i(k)$  is the power spectrum estimator of the  $i$ -th realization and  $P(k; \mathbf{x})$  is its mean. For this analysis we simply use the real-space power spectrum.

The variation in the power spectrum around the fiducial model can be expressed as

$$P(k; \mathbf{x}) \simeq P(k; \mathbf{x}_{\text{fid}}) + \left. \frac{\partial P(k; \mathbf{x})}{\partial \mathbf{x}} \right|_{\text{fid}} \cdot (\mathbf{x} - \mathbf{x}_{\text{fid}}). \quad (7)$$

Recall that the best-fit parameters are estimated by minimizing the  $\chi^2$ . The best-fit parameters for the  $i$ -th realization can be estimated by inserting Eq. (7) into Eq. (6) (e.g. Huterer & Takada 2005; Joachimi & Schneider 2009):

$$(\mathbf{x}_{\text{bf}} - \mathbf{x}_{\text{fid}})_i = \sum_j (F^{-1})_{ij} \sum_{k_1, k_2 < k_{\max}} \text{cov}^{-1}(k_1, k_2) \times [P_i(k_1) - P(k_1, \mathbf{x}_{\text{fid}})] \left. \frac{\partial P(k_2; \mathbf{x})}{\partial x_j} \right|_{\text{fid}}. \quad (8)$$

Thus the best-fit parameters are generally different from the fiducial values depending on the distribution of  $P_i$  or how  $P_i$  deviates from the ensemble average expectation  $P$  at each wavenumber. Strictly speaking, we need to vary the covariance as a function of cosmological models in Eq. (8), but we here simply employ the covariance for the fiducial model assuming that the variations in the covariance are small (see Eifler, Schneider & Hartlap 2009 for this issue).

Fig.4 shows how the best-fit values of  $w$  are distributed among 5000 realizations. Note that, as can be seen in Eq. (8), the dark energy constraint includes the power spectrum amplitude information in addition to the BAO features. The left-panel shows the result for one parameter fitting ( $w$ ), while the right panel for the three parameter fitting ( $w, A_s, n_s$ ), where the best-fit  $w$  is derived by including marginalization over the two parameters ( $A_s, n_s$ ). The latter corresponds to the case that the other parameters ( $\Omega_c h^2, \Omega_b h^2$ ) are well constrained by external information such as the CMB and/or the Big Bang Nucleosynthesis (BBN). The red (black) curve shows the result obtained when the non-Gaussian errors in the Fisher matrix and the covariance in Eq. (8) are included (not included). The corresponding best-fit parameter deviations are plotted in the unit,  $[(w/w_{\text{fid}}) - 1]/\sigma$ , where  $\sigma$  is set to the Fisher errors with and without the non-Gaussian errors for the red and black curves, respectively. For example, the parameter deviations  $|(w/w_{\text{fid}}) - 1|/\sigma \leq 3$  mean that the parameter deviations are within  $\pm 3\sigma$  confidence level regions.

The distribution of the best-fit  $w$  looks nearly symmetric: the nonlinear power spectrum does not shift the  $w$ -parameter to either of negative and positive sides from the fiducial value. The left panel (one-parameter fitting case) shows that including only the Gaussian errors makes the distribution of the best-fit  $w$  broader than the statistical confidence region. Clearly, a strong evidence on  $w \neq -1$  may be incorrectly derived with high chances under the Gaussian assumptions. However, the red curves demonstrate that such apparent deviations can be corrected if we properly take into account the non-Gaussian errors for the statistical confidence regions. The right panel shows that, for a multi-parameter fit, the difference between the results with and without the non-Gaussian errors is significantly suppressed due to the parameter degeneracies. Note that our results in Fig.4 is independent of the assumed survey volume, because  $[w/(w_{\text{fid}}) - 1] \propto V^{-1/2}$  from Eq.(8) and  $\sigma \propto V^{-1/2}$ . Although we show the result only for  $w$ , essentially the same results are obtained for other parameters ( $A_s, n_s, \Omega_b h^2, \Omega_c h^2$ ).

In Fig.5, we quantify how the best-fit values of  $w$  are systematically different when including or ignoring the non-Gaussian errors. The horizontal axis is the difference between the best-fit parameters,  $(w_G - w_{\text{NG}})/w_{\text{fid}}$ , divided by the  $1\sigma$  statistical confidence error derived by including the non-Gaussian errors. The left panel shows that the differences are smaller than the  $1\sigma$  confidence regions, and the right panels show even much smaller differences for the three-parameter fitting. Therefore we again conclude that the non-Gaussian errors do not cause any significant bias in the best-fit value compared to the statistical confidence regions including the non-Gaussian

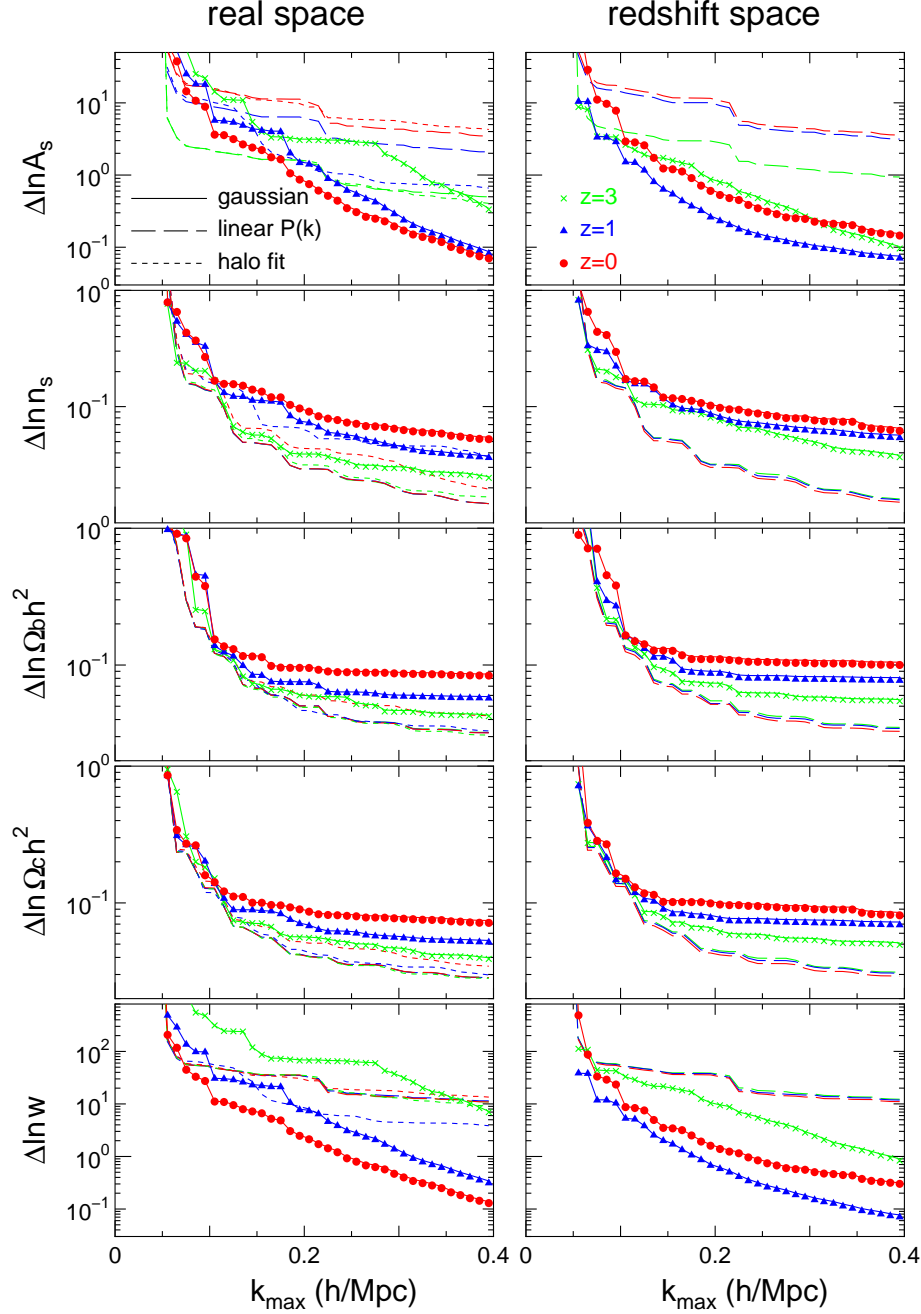


FIG. 2.— The marginalized errors of each parameter when including the power spectrum information up to the maximum wavenumber  $k_{\max}$  in the horizontal axis. The left- and right panels show the results for the real- and redshift-space, respectively. The symbols in each panel are as for the previous figures. The solid curves which lie almost on top of the symbols show the results obtained only by including the Gaussian errors in the Fisher analysis. The agreement indicates that the Gaussian error assumption is a good approximation for parameter estimations even at small scales (see text for the details). The dashed and dotted curves are the analytical predictions that are derived using the linear theory and halo fit for the power spectrum and the Gaussian covariance, respectively.

errors.

#### 4. ACOUSTIC PEAK POSITIONS

A more robust method to constrain dark energy is using the BAO peak positions. The BAO peak positions are characterized basically by *one* parameter, the stretch parameter (see below), and therefore the non-Gaussian errors may significantly affect the accuracy of the peak position determination. Here we use the distribution of the BAO peak positions obtained from our 5000 real-

izations. We employ the method developed in Percival et al. (2007) to estimate the peak positions (see also Nishimichi et al. 2009). We first divide the measured  $P(k)$  by a smooth model, which is constructed by adopting the cubic B-spline function to fit the binned power spectrum over a range of wavenumbers binned with the width  $\Delta k = 0.01 h/\text{Mpc}$ .

Fig.6 shows the power spectrum divided by the smooth model: the data points are the average spectrum of 5000 realizations and the errors the  $1\sigma$  variation ranges,

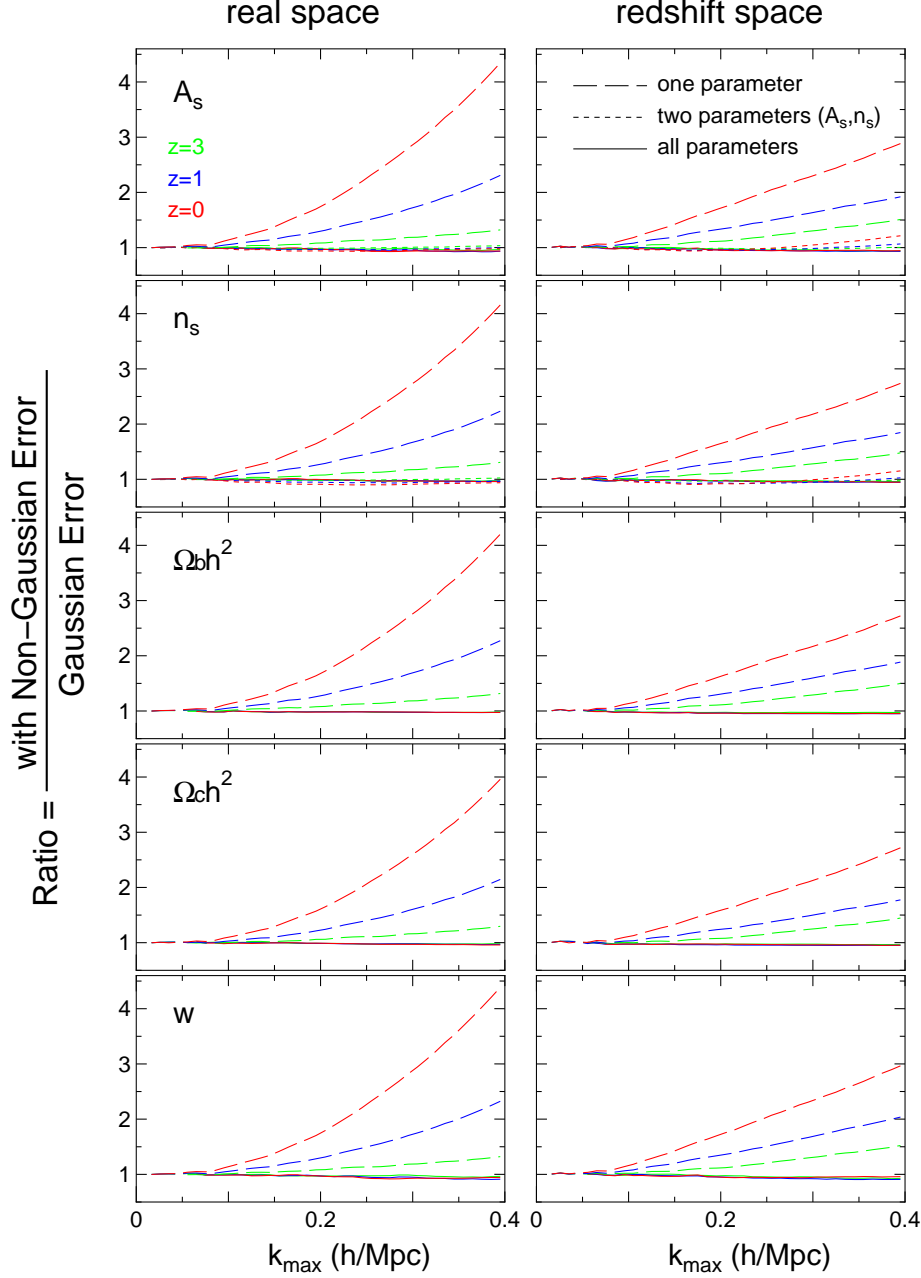


FIG. 3.— The ratio of the marginalized errors with and without the non-Gaussian errors, as a function of  $k_{\max}$ . The solid curves show the results for our fiducial set of five cosmological parameters as shown in each panel. For comparison the dashed curves show the results for the unmarginalized errors or equivalently for the case of one parameter fitting in each panel. Also in the panels for  $A_s$  and  $n_s$  the dotted curves show the results for the two parameter fitting of  $(A_s, n_s)$ , which appear to be between the solid and dashed curves. It is clear that the non-Gaussian errors degrade the unmarginalized errors by up to a factor 5.

$\Delta P(k) = \text{cov}^{1/2}(k, k)$ . Clearly, the BAO features are smoothed out at larger  $k$  and at lower redshifts due to stronger nonlinearities.

To make parameter forecasts, let us define the ratio power spectrum,  $R(k)$ , as

$$R(k) = \frac{P(k)}{P_{\text{smooth}}(k)}. \quad (9)$$

Then we can introduce the stretch parameter  $\alpha$  which characterizes a shift of the BAO peak phases via the transform  $k \rightarrow \alpha k$  in  $R(k)$ . The power spectrum with

the stretch parameter  $\alpha$  is given as

$$P(k; \alpha) = P_{\text{smooth}}(k) R(\alpha k), \quad (10)$$

and  $\alpha = 1$  is the fiducial model. The Fisher information matrix for the stretch parameter  $\alpha$  is computed as

$$F_{\alpha\alpha} = \sum_{k_{1,2} < k_{\max}} \text{cov}^{-1}(k_1, k_2) \frac{dP(k_1; \alpha)}{d\alpha} \frac{dP(k_2; \alpha)}{d\alpha}. \quad (11)$$

Since we focus on the BAO peak locations, we treat only  $\alpha$  as a free parameter, and hence the precision of determining  $\alpha$  for the given power spectrum measurement is given as  $\Delta\alpha = F_{\alpha\alpha}^{-1/2}$ .

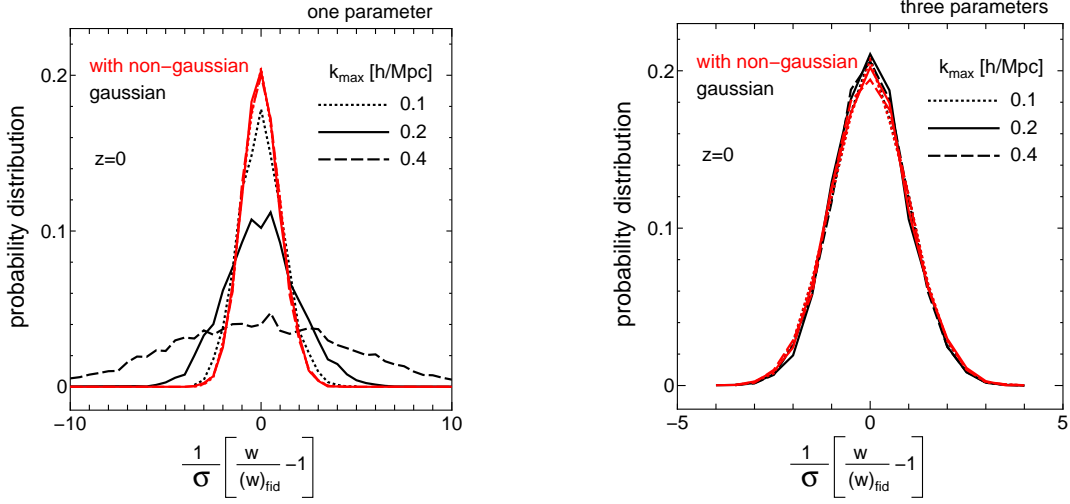


FIG. 4.— The distribution of the best-fit parameter  $w$  estimated for the power spectra of 5000 realizations in real space. The red (black) curve shows the result obtained with (without) the non-Gaussian error covariance in Eq. (8). The dotted, solid and dashed curves are for  $k_{\max} = 0.1, 0.2$  and  $0.4 h/\text{Mpc}$ , respectively. The left panel shows the best-fit values of  $w$  for one parameter fitting ( $w$  alone), while the right panel shows the results for three parameter fitting ( $w, A_s, n_s$ ). The horizontal axis is defined as  $(w/w_{\text{fid}} - 1)/\sigma$ , where  $\sigma$  denotes the  $1\sigma$  confidence regions computed from the Fisher matrix with and without the non-Gaussian errors for the red and black curves, respectively.

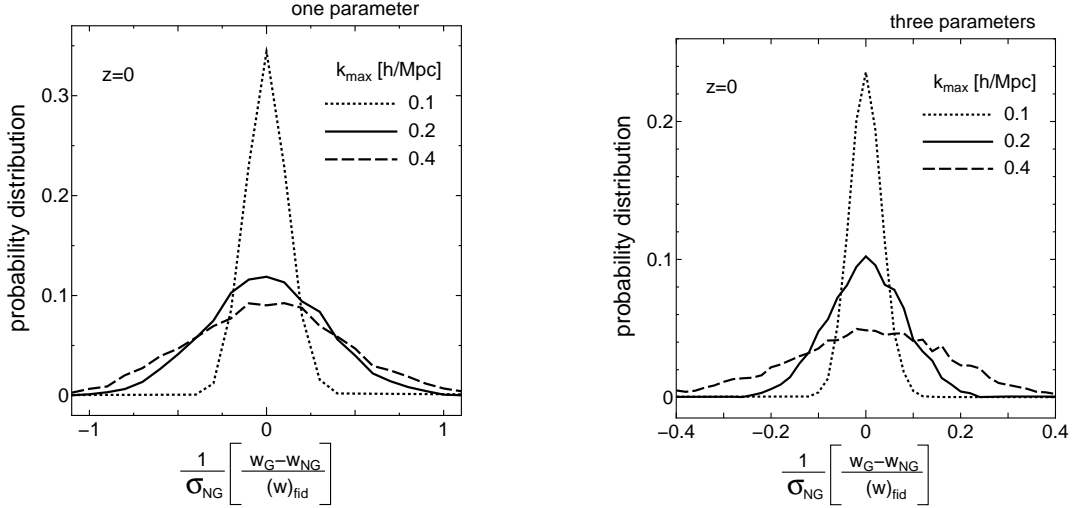


FIG. 5.— As for the previous figures, but for the distribution of the differences between the best-fit values of  $w$  computed from Eq. (8) with and without non-Gaussian errors. The  $\sigma_{\text{NG}}$  is the  $1\sigma$  error computed from the Fisher matrix with the non-Gaussian errors.

Fig.7 shows the  $1\sigma$  error,  $\Delta\alpha$ , as a function of  $k_{\max}$  up to which the power spectrum information is included. The symbols are the results including the non-Gaussian errors in the Fisher analysis, while the solid curves are for the Gaussian errors. The Gaussian error assumption appears to be valid even for large  $k_{\max}$ . This is because the BAO features are erased at the weakly nonlinear scales  $k > 0.2 h/\text{Mpc}$ , where the non-Gaussian errors are more significant. There is little information on the acoustic scale at the nonlinear scales. At  $z = 0$  the accuracy improves significantly around the first peak ( $k \sim 0.06 h/\text{Mpc}$ ) and the second peak ( $k \sim 0.12 h/\text{Mpc}$ ). Hence almost all the information on the acoustic peaks are obtained for  $k \lesssim 0.15 h/\text{Mpc}$  at  $z = 0$ . From Fig.7,  $\Delta\alpha \sim 1\%$  can be achievable for a survey with  $(\text{Gpc}/h)^3$  volume coverage.

Finally, we investigate the distribution of best-fit  $\alpha$

among 5000 realizations. Given the power spectrum measurement for the  $i$ -th realization, the  $\chi^2$  for estimating  $\alpha$  is given as

$$\chi_i^2(\alpha) = \sum_{k_1, k_2 < k_{\max}} \text{cov}^{-1}(k_1, k_2) P_{\text{smooth}}(k_1) P_{\text{smooth}}(k_2) \times [R(\alpha k_1) - \hat{R}_i(k_1)] [R(\alpha k_2) - \hat{R}_i(k_2)]. \quad (12)$$

Here, we have used the power spectrum  $P_i(k)$  for the  $i$ -th realization, not the mean  $P(k)$ , to obtain the smooth power spectrum in the denominator of the ratio  $\hat{R}_i(k)$ ,

Fig.8 shows the distribution of the best-fit shift parameters  $\alpha$  for the cases of  $k_{\max} = 0.2$  and  $0.4 h/\text{Mpc}$ . The horizontal axis is  $\alpha - 1$  divided by the  $1\sigma$  error  $\sigma_\alpha$  obtained by the Fisher matrix. The red curves are the results including the non-Gaussian errors, while the black curves are for the Gaussian errors. The two results are in-



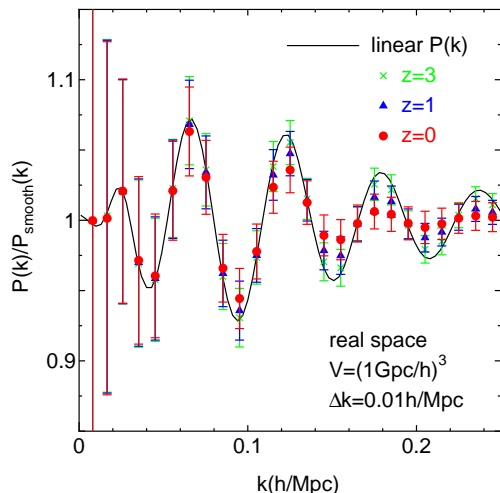


FIG. 6.— The real-space power spectrum divided by the smoothed spectrum for  $z = 0, 1$  and  $3$ , respectively. The symbols denote the mean of the power spectra among 5000 realizations of  $(1h/\text{Gpc})^3$  volume, while the error bars denote the  $1\sigma$  scatters. The solid curve is for the linear  $P(k)$ . The BAO features are more erased at higher  $k$  and at lower redshifts due to stronger nonlinearities.

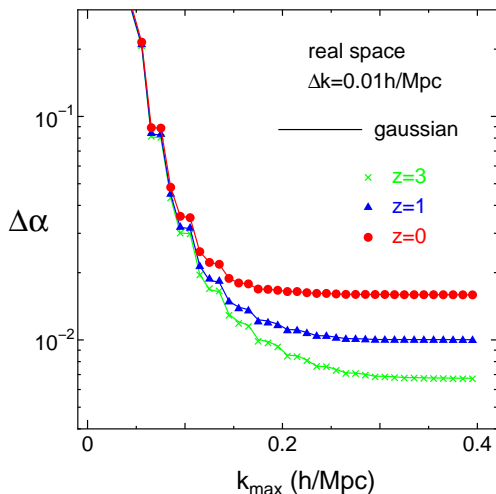


FIG. 7.— The  $1\sigma$  error on the BAO peak position parametrized by the stretch parameter  $\alpha$  (see text for the definition). The symbols are the results computed from simulations, while the solid curves, which are almost top on the symbols, show the errors computed assuming the Gaussian errors.

deed very similar. The distribution is well described by a Gaussian function with the width given by the  $1\sigma$  Fisher error. A recent work by Seo et al. (2009) compares the distribution of the acoustic scales with the result from the Fisher matrix analysis. Although their analysis is slightly different from ours (they use a fitting formula for the non-linear  $P(k)$  when calculating the acoustic scale), their results are broadly consistent with the results shown here.

Fig.9 shows the difference between the best-fit shift parameters when including or ignoring the non-Gaussian errors in Eq.(12). The difference is smaller than  $\sim 0.2\sigma$ .

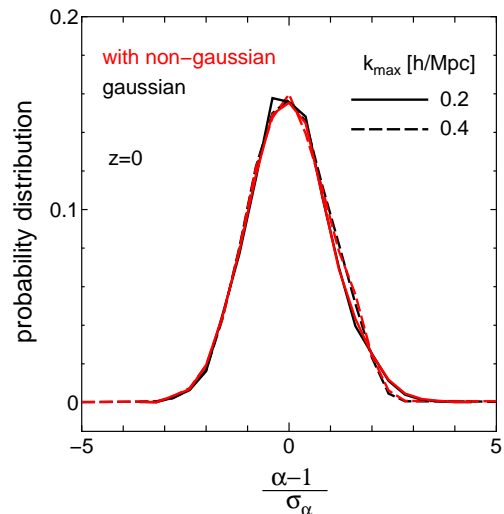


FIG. 8.— The distribution of the shift parameter  $\alpha$  for  $k_{\text{max}} = 0.2$  (solid curves) and  $0.4h/\text{Mpc}$  (dashed curves), respectively. The horizontal axis  $\alpha - 1$  is divided by the  $1\sigma$  error computed from the Fisher matrix. The red and black curves are the results with and without the non-Gaussian errors, respectively. The distribution of  $\alpha$  is well described by a Gaussian distribution with the width of the  $1\sigma$  Fisher error.

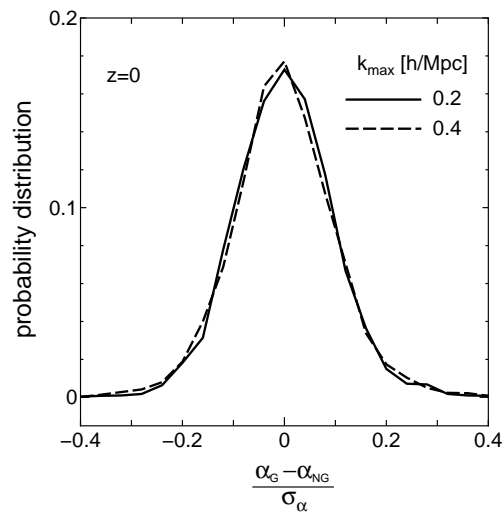


FIG. 9.— The distribution of the differences between the best-fit values of  $\alpha$  with or without including the non-Gaussian covariance. The solid (dashed) curve is for  $k_{\text{max}} = 0.2(0.4)h/\text{Mpc}$ .

Hence we conclude that the non-Gaussian covariance does not cause a substantial systematic error in the BAO peak determination.

## 5. DISCUSSION AND CONCLUSION

We have studied the effects of the non-Gaussian error on the parameter estimations and the distribution of the best-fit parameters for the cosmological parameters (in section 3) and the acoustic scale position (in section 4). We have found that the non-Gaussian error is important for the parameter errors if there is only one fitting parameter. The measurement error degrades up

to factor 5 for  $k_{\max} = 0.4$ . However, if there are more than two parameters, the impact of the non-Gaussian errors are insignificant due to severe parameter degeneracies in the matter power spectrum. For the acoustic scale, the non-Gaussian errors do not affect the acoustic scale determination, even though there is only one fitting parameter. This is because that the acoustic scale is determined mainly by the linear scales where the non-Gaussian covariance is not important.

Throughout this paper, we discussed the covariance matrix of the matter power spectrum. However, for real galaxy survey, we should include the effects of the halo and galaxy bias. However addressing this issue is not easy at present, because we need the large number of realizations of high resolution simulations including halo and galaxy formation. For large scale ( $k \lesssim 0.1h/\text{Mpc}$ ), the covariance of the halo power spectrum is consistent with the Gaussian error with the shot noise term (Angulo et al. 2008; Smith 2009). Because, in the linear regime, only the sample variance dominates the covariance. For small scale ( $k > 0.1h/\text{Mpc}$ ), Smith (2009) recently showed that the covariance is larger than the Gaussian error predic-

tion and the higher mass halo have stronger covariance due to the non-linear gravitational mode coupling. He compared the cluster-sized halos in the two mass ranges ( $M > 10^{14}M_\odot$  and  $1 \times 10^{13}M_\odot < M < 2 \times 10^{13}M_\odot$ ), and hence we expect the galactic halo ( $M \lesssim 10^{13}M_\odot$ ) would have a weaker covariance.

In our previous paper (T09), we compare the power spectrum covariance in numerical simulations with an analytical models such as perturbation theory and halo model. We calculated the diagonal and off-diagonal terms of the covariance matrix and the signal-to-noise ratio in the both models, and found that the halo model reasonably well reproduces the simulation results. Several authors also compare them and reached the same conclusion (e.g. Cooray & Hu 2001; Neyrinck et al. 2006; Neyrinck & Szapudi 2007; Sato et al. 2009).

Our simulation results of the 5000 power spectra  $P_i(k)$ , the derivative of  $P(k)$  with respect to the cosmological parameters,  $\partial P(k)/\partial x_j$ , and the covariance matrix  $\text{cov}(k_1, k_2)$  are available as numeric tables upon request (contact takahasi@cc.hirosaki-u.ac.jp).

## APPENDIX

### VARIANCE OF THE COVARIANCE MATRIX FOR THE GAUSSIAN DENSITY FLUCTUATIONS

The covariance matrix estimated from  $N_r$  realizations is given by,

$$\begin{aligned} \text{cov}(k_1, k_2; N_r) &= \frac{1}{N_r} \sum_i \left[ \hat{P}_i(k_1) - \bar{P}(k_1) \right] \left[ \hat{P}_i(k_2) - \bar{P}(k_2) \right], \\ &= \frac{1}{N_r} \sum_i \hat{P}_i(k_1) \hat{P}_i(k_2) - \frac{1}{N_r} \sum_i \hat{P}_i(k_1) \frac{1}{N_r} \sum_j \hat{P}_j(k_2). \end{aligned} \quad (\text{A1})$$

The variance of the covariance is given by,

$$\begin{aligned} \text{var}[\text{cov}(k_1, k_2; N_r)] &\equiv \langle \text{cov}^2(k_1, k_2; N_r) \rangle - \langle \text{cov}(k_1, k_2; N_r) \rangle^2 \\ &= \frac{1}{N_r^2} \sum_{i,j} \left[ \langle \hat{P}_i(k_1) \hat{P}_i(k_2) \hat{P}_j(k_1) \hat{P}_j(k_2) \rangle - \langle \hat{P}_i(k_1) \hat{P}_i(k_2) \rangle \langle \hat{P}_j(k_1) \hat{P}_j(k_2) \rangle \right] \\ &\quad - \frac{2}{N_r^3} \sum_{i,j,k} \left[ \langle \hat{P}_i(k_1) \hat{P}_i(k_2) \hat{P}_j(k_1) \hat{P}_k(k_2) \rangle - \langle \hat{P}_i(k_1) \hat{P}_i(k_2) \rangle \langle \hat{P}_j(k_1) \hat{P}_k(k_2) \rangle \right] \\ &\quad + \frac{1}{N_r^4} \sum_{i,j,k,l} \left[ \langle \hat{P}_i(k_1) \hat{P}_j(k_2) \hat{P}_k(k_1) \hat{P}_l(k_2) \rangle - \langle \hat{P}_i(k_1) \hat{P}_j(k_2) \rangle \langle \hat{P}_k(k_1) \hat{P}_l(k_2) \rangle \right], \end{aligned} \quad (\text{A2})$$

The above equation further reduces to

$$\begin{aligned} \text{var}[\text{cov}(k_1, k_2; N_r)] &= \frac{1}{N_r} \left[ \langle \hat{P}^2(k_1) \hat{P}^2(k_2) \rangle - \langle \hat{P}(k_1) \hat{P}(k_2) \rangle^2 \right] \\ &\quad - \frac{2}{N_r} \left[ \langle \hat{P}^2(k_1) \hat{P}(k_2) \rangle \langle \hat{P}(k_2) \rangle - \langle \hat{P}(k_1) \hat{P}(k_2) \rangle \langle \hat{P}(k_1) \rangle \langle \hat{P}(k_2) \rangle + (k_1 \leftrightarrow k_2) \right] \\ &\quad + \frac{1}{N_r} \left[ \left( \langle \hat{P}^2(k_1) \rangle - \langle \hat{P}(k_1) \rangle^2 \right) \langle \hat{P}(k_2) \rangle^2 + (k_1 \leftrightarrow k_2) \right] \\ &\quad + \frac{2}{N_r} \left[ \langle \hat{P}(k_1) \hat{P}(k_2) \rangle - \langle \hat{P}(k_1) \rangle \langle \hat{P}(k_2) \rangle \right] \langle \hat{P}(k_1) \rangle \langle \hat{P}(k_2) \rangle \end{aligned} \quad (\text{A3})$$

Here we ignored the terms of the order of  $(1/N_r)^2$  and higher.

For the Gaussian density fluctuations, the  $n$ -th moments  $\langle \hat{P}^n \rangle$  can be obtained using the probability distribution function of  $P(k)$  (the chi-squared distribution function, see Eq.(B1) in T09). For the diagonal parts, we have

$$\text{var}[\text{cov}(k_1, k_1; N_r)] = \frac{1}{N_r} \left( \frac{8}{N_k^2} + \frac{48}{N_k^3} \right) \simeq \frac{8}{N_r N_k^2} P^4(k) \quad (\text{A4})$$

Hence we have

$$\frac{\text{var}[\text{cov}(k_1, k_1; N_r)]}{\text{cov}^2(k_1, k_1)} = \frac{2}{N_r} \quad (\text{A5})$$

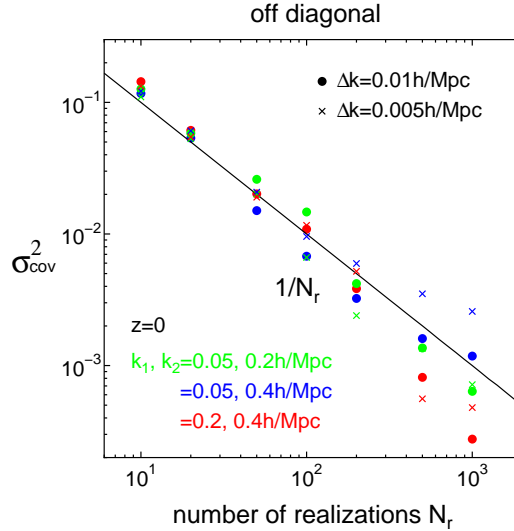


FIG. 10.— The dispersions among the power spectrum covariances each of which is estimated from the  $N_r$  realizations (a subset of the while 5000 realizations), as a function of  $N_r$ . In the vertical axis, the dispersion is defined in Eq. (A7). The panel shows the result for the off-diagonal parts for varying the wavenumber bins and the bin widths. The color symbols are the simulation results, while the solid curves denote the theoretical prediction for the Gaussian density fluctuation. The plots explicitly show that the power spectrum covariances are estimated at a sub-percent level accuracy by using our whole 5000 realizations.

which is consistent with our numerical finding in our previous paper (see left panel of Fig.12 in T09). Hence if we need 10%(5%) accuracy in the covariance, we have to prepare 200(800) realizations.

For the off-diagonal parts we have

$$\text{var} [\text{cov}(k_1, k_2; N_r)] = \frac{1}{N_r} \frac{2}{N_{k_1}} \frac{2}{N_{k_2}} P^2(k_1) P^2(k_2) \quad (\text{A6})$$

Let us define the relative errors as,

$$\sigma_{cov}^2 = \frac{\text{var} [\text{cov}(k_1, k_2; N_r)]}{\text{cov}(k_1, k_1) \text{cov}(k_2, k_2)}. \quad (\text{A7})$$

In Fig.10, we show the relative errors  $\sigma_{cov}^2$  in Eq.(A7) as a function of  $N_r$ . The solid line is the theoretical prediction in Eq.(A7), and the symbols are the results of our numerical simulation for various scales ( $k = 0.05, 0.2, 0.4 h/\text{Mpc}$ ) and bin-width ( $\Delta k = 0.005, 0.01 h/\text{Mpc}$ ). Analytical results in Eq.(A6) fit our simulation data well.

We would like to thank Daniel Eisenstein and Hee-Jong Seo for useful comments and discussions. This work is supported in part by Grant-in-Aid for Scientific Research on Priority Areas No. 467 “Probing the Dark Energy through an Extremely Wide and Deep Survey with Subaru Telescope”, by the Grand-in-Aid for the Global COE Program “Quest for Fundamental Principles in the Universe: from Particles to the Solar System and the Cosmos” from the Ministry of Education, Culture, Sports, Science and Technology (MEXT) of Japan, by the World Premier International Research Center Initiative of MEXT of Japan, by the Mitsubishi Foundation, and by Japan Society for Promotion of Science (JSPS) Core-to-Core Program “International Research Network for Dark Energy”, and by Grant-in-Aids for Scientific Research (Nos. 18740132, 18540277, 18654047). I.K., T.N. and S.S. are supported by Grants-in-Aid for Japan Society for the Promotion of Science Fellows. A.T. is supported in part by a Grants-in-Aid for Scientific Research from the JSPS (No. 21740168).

## REFERENCES

- Alcock, C. & Paczynski, B., 1979, *Nature*, 281, 358  
Angulo, R.E., Baugh, C.M., Frenk, C.S., & Lacey, C.G., 2008, *MNRAS*, 383, 755  
Blake, C. & Glazebrook, K., 2003, *ApJ*, 594, 665  
Cole, S., et al., 2005, *MNRAS*, 362, 505  
Cooray, A. & Hu, W., 2001, *ApJ*, 554, 56  
Croce, M. & Scoccimarro, R., 2006, *PRD*, 73, 063519  
Croce, M. & Scoccimarro, R., 2008, *PRD*, 77, 023533  
Dore, O., Lu, T. & Pen, U.-L., 2009, arXiv:0905.0501, submitted to PRD  
Eifler, T., Schneider, P. & Hartlap, J., 2008, submitted to A&A, arXiv:0810.4254  
Eisenstein, D.J., Hu, W. & Tegmark, M., 1998, *ApJ*, 504, L57  
Eisenstein, D.J. et al., 2005, *ApJ*, 633, 560  
Eisenstein, D.J., Seo, H.-J., Sirko, E. & Spergel, D.N., 2007 *ApJ*, 664, 675  
Feldman, H.A., Kaiser, N. & Peacock, J.A., 1994, *ApJ*, 426, 23  
Gaztanaga, E., Cabre, A. & Hui, L., 2008, arXiv:0807.3551  
Guzik, J., Bernstein, G. & Smith, R.E., 2007, *MNRAS*, 375, 1329  
Hamilton, A.J.S., Rimes, C.D. & Scoccimarro, R., 2006, *MNRAS*, 371, 1188  
Hartlap, J., Schrabback, T., Simon, P., & Schneider, P., 2009, arXiv:0901.3269, accepted for publication in A & A  
Heitmann, K., 2009, arXiv:0812.1052  
Huff, E., et al., 2007, *Astroparticle Physics*, 26, 351  
Huterer, D. & Takada, M., 2005, *Astroparticle Physics*, 23, 369  
Ichiki, K., Takada, M. & Takahashi, T., 2009, *PRD*, 79, 023520  
Jeong, D. & Komatsu, E., 2006, *ApJ*, 651, 619  
Jeong, D. & Komatsu, E., 2009, *ApJ*, 691, 569

- Joachimi, B. & Schneider, P., 2009, arXiv:0905.0393, submitted to A & A
- Kazin et al., 2009, arXiv:0908.2598, submitted to ApJ
- Kim, J., Park, C., Gott III, J.R., & Dubinski J., 2009, ApJ, 701, 1547
- Komatsu, E., et al., 2009, ApJS, 180, 330
- Lee, J. & Pen, U.-L., 2008, ApJL, 686, 1
- Lewis, A., Challinor, A. & Lasenby, A., 2000, ApJ, 538, 473
- Lu, T., Pen, U.-L., Dore, O., 2009, arXiv:0905.0499, submitted to PRD
- Matarrese, S. & Pietroni, M., 2007, JCAP 0706:026
- Matarrese, S. & Pietroni, M., 2008, Mod. Phys. Lett. A, 23, 25
- Matsubara, T., 2004, ApJ, 615, 573
- Matsubara, T., 2008a, PRD, 77, 063530
- Matsubara, T., 2008b, PRD, 78, 083519
- Meiksin, T., White, M. & Peacock, J.A., 1999, MNRAS, 304, 851
- Meiksin, T. & White, M., 1999, MNRAS, 308, 1179
- McDonald, P., 2007, PRD, 75, 043514
- Neyrinck, M.C., Szapudi, I. & Rimes, C.D., 2006, MNRAS, 370, L66
- Neyrinck, M.C. & Szapudi, I., 2007, MNRAS, 375, L51
- Neyrinck, M.C. & Szapudi, I., 2008, MNRAS, 384, 1221
- Neyrinck, M.C., Szapudi, I. & Szalay, A.S., 2009, arXiv:0903.4693
- Nishimichi, T., et al., 2007, PASJ, 59, 1049
- Nishimichi, T., et al., 2009, PASJ, 61, 321
- Nomura, H., Yamamoto, K. & Nishimichi, T., 2008, JCAP, 10, 031
- Okumura, T., et al., 2008, ApJ, 676, 889
- Padmanabhan, N. & White, M., 2008, PRD, 77, 123540
- Percival, W.J., et al., 2007, MNRAS, 381, 1053
- Percival, W.J., et al., 2009, submitted to MNRAS, arXiv:0907.1660
- Pielorz, J., Rodiger, J., Tereno, I. & Schneider, P., 2009, arXiv:0907.1524, submitted to A & A
- Pietroni M., 2008, JCAP 0810:036
- Rassat, A. et al., 2008, submitted to MNRAS, arXiv:0810.0003
- Reid, B.A., et al., 2009, submitted to ApJ, arXiv:0907.1659
- Rimes, C.D. & Hamilton, A.J.S., 2005, MNRAS, 360, L82
- Rimes, C.D. & Hamilton, A.J.S., 2006, MNRAS, 371, 1205
- Saito, S., Takada, M. & Taruya, A., 2009, PRD, 80, 083528
- Sanchez, A.G., Baugh, C.M. & Angulo, R., 2008, MNRAS, 390, 1470
- Sanchez, A.G., et al., 2009, submitted to MNRAS, arXiv:0901.2570
- Sato, M. et al., 2009, ApJ, 701, 945
- Scoccimarro, R., Zaldarriaga, M. & Hui, L., 1999, ApJ, 527, 1
- Sefusatti, E., Crocce, M., Pueblas, S. & Scoccimarro, R., 2006, PRD, 74, 023522
- Seljak, U., Zaldarriaga, M., 1996, ApJ, 469, 437
- Seo, H.J. & Eisenstein, D.J., 2003, ApJ, 598, 720
- Seo, H.J. & Eisenstein, D.J., 2005, ApJ, 633, 575
- Seo, H.J. Siegel, E.R., Eisenstein, D.J. & White M., 2008, ApJ, 686, 13
- Seo, H.J., et al., 2009, submitted to ApJ, arXiv:0910.5005
- Shoji, M., Jeong, D. & Komatsu, E., 2009, ApJ, 693, 1404
- Smith, R.E., et al. 2003, MNRAS, 341, 1311
- Smith, R.E., Scoccimarro, R. & Sheth, R.K., 2007, PRD, 75, 3512
- Smith, R.E., Scoccimarro, R. & Sheth, R.K., 2008, PRD, 77, 3525
- Spergel, D.N., et al., 2007, ApJ, 170, 377
- Springel, V., Yoshida, N. & White, S.D.M., 2001, New Astronomy, 6, 79
- Springel, V., 2005, MNRAS, 364, 1105
- Takada, M. & Jain, B., 2009, MNRAS, 395, 2065
- Takahashi, R., et al., 2008, MNRAS, 389, 1675
- Takahashi, R., 2008, Progress of Theoretical Physics, 120, 549
- Takahashi, R. et al., 2009, ApJ, 700, 479
- Taruya, A. & Hiramatsu, T., 2008, ApJ, 674, 617
- Taruya, A., Nishimichi, T., Saito, S. & Hiramatsu, T., 2009, PRD 80, 123503
- Tegmark, M., Taylor, A.N. & Heavens, A.F., 1997, ApJ, 480, 22